

Numerical Simulation of Laminar Film Cooling in a Supersonic Boundary Layer using Modeled and Simulated Blowing

By **M. Keller** AND **M.J. Kloker**

Institut für Aerodynamik und Gasdynamik, Universität Stuttgart
Pfaffenwaldring 21, 70569 Stuttgart

Direct numerical simulations are used to investigate the method of film cooling in a laminar flat-plate Mach-2.67 boundary layer. Air is employed as mean-flow and coolant gas and is injected into an adiabatic or isothermal boundary layer through one or two rows of staggered, discrete holes. Previous simulations were performed using a modeled blowing approach, where the mass flux and temperature distribution are prescribed by a 5th-order polynomial. This work is dedicated to the simulation of film cooling using additional cylindrical computational domains which represent the blowing channels, enabling a validation of the modeled blowing. It is shown that the temperature modeling plays a significant role for the adiabatic-wall boundary condition. Also, it is demonstrated that for the blowing through two rows of staggered holes the mass-flux through the first row is notably lower than through the second row. Note that the same plenum pressure is assumed for both rows. The holes are acting as obstacles in the flow, leading to an increase of the wall pressure in front of them. As a result, the driving pressure difference between the plenum and the freestream is reduced for the first row.

1. Introduction

In order to protect the thermally highly loaded regions of combustion chambers and rocket nozzles of next-generation space transportation systems innovative and efficient cooling strategies have to be developed. A promising ansatz is the method of film cooling which is a viable cooling technique in high speed flows and perfectly suited for active thermal protection systems.

The influence of film cooling through discrete holes and spanwise slits on laminar super- and hypersonic boundary layers has been investigated, among others, extensively by Linn & Kloker, see e.g. [1–3]. Direct numerical simulations were used to analyze the effects of geometric and gas-dynamic parameters, such as hole spacing, hole arrangement, Mach number, Reynolds number, blowing ratio, inclination angle, compound angle and wall-temperature condition. From a cooling-performance point of view, slits are better than holes when imposing the same total mass flux, and staggered hole rows are better than aligned rows. Also, a small spanwise spacing is preferable in order to generate a more homogeneous cooling film. It was furthermore demonstrated that the wall-temperature condition – isothermal, adiabatic or radiative-adiabatic – as well as an inclination angle and compound angle strongly affect the cooling performance. Corresponding experimental studies have been performed by Heufer, Hombsch & Olivier,

see e.g. [4–6]. They investigated the effects of spanwise slits and discrete holes as well as the influence of the blowing ratio, Mach number, Reynolds number, various coolant gases, and flow acceleration. A comparison of the numerical results with the experimental findings for a laminar Mach-2.67 boundary layer with an isothermal wall and spanwise slits showed good agreement [1].

Numerical investigations of film cooling in a supersonic boundary layer at Mach 2.6 were also performed by Dahmen, Gotzen & Müller, e.g. [7]. The authors are using a multi-resolution finite-volume solver in order to develop new multi-scale techniques for highly resolved vortical structures.

The modeling of the cooling gas injection plays an important role in the numerical investigation of film cooling. In order to evaluate its influence on the developing flow structures and the cooling effectiveness a comparison with a simulated blowing approach is presented. Here, an additional cylindrical computational domain per hole representing the cylindrical blowing channel is considered in the simulations. The remainder of this paper is organized as follows: Chapter 2 describes the governing equations and the numerical procedure, boundary conditions, and simulation setup of the problem. The results are presented in Chapter 3. Finally, Chapter 4 summarizes the main findings and contains some concluding remarks.

2. Numerical Method

2.1. Governing equations

The governing equations are the continuity equation, the three-dimensional compressible Navier-Stokes equations and the energy equation, in the following written in dimensionless vectorized form:

$$\frac{\partial \rho}{\partial t} + \nabla \cdot (\rho \vec{v}) = 0 \quad , \quad (2.1)$$

$$\frac{\partial (\rho \vec{v})}{\partial t} + \nabla \cdot (\rho \vec{v} \vec{v}) + \nabla p = \frac{1}{Re} \cdot \nabla \vec{\sigma} \quad \text{and} \quad (2.2)$$

$$\frac{\partial (\rho e)}{\partial t} + \nabla \cdot (p + \rho e) \vec{v} = \frac{1}{(\kappa - 1) Re Pr Ma^2} \nabla \cdot (\vartheta \nabla T) + \frac{1}{Re} \nabla \cdot (\vec{\sigma} \vec{v}) \quad , \quad (2.3)$$

where

$$\vec{\sigma} = \mu \left((\nabla \vec{v} + \nabla \vec{v}^T) - \frac{2}{3} (\nabla \cdot \vec{v}) \mathbf{I} \right) \quad (2.4)$$

describes the viscous stresses and

$$e = c_v \cdot T + \frac{1}{2} (u^2 + v^2 + w^2) \quad (2.5)$$

is the internal energy per mass unit. The governing equations are non-dimensionalized with the reference length $L^* = (\mu_\infty^* \cdot Re) / (\rho_\infty^* \cdot u_\infty^*)$ and the freestream values of velocity, density, temperature, viscosity and conductivity at the inflow. Note that the pressure is non-dimensionalized with $(\rho_\infty^* u_\infty^{*2})$. Air is treated as a non-reacting calorically perfect gas with constant Prandtl number $Pr = 0.71$ and constant specific-heat ratio $\kappa = c_p / c_v = 1.4$. The set of equations is closed by the equation of state $p = (\rho T) / (\kappa Ma^2)$. Sutherland's law is used to calculate the dynamic viscosity μ as a function of temperature [8]. In these equations, $\vec{v} = (u, v, w)^T$ represents the velocity vector, p labels the

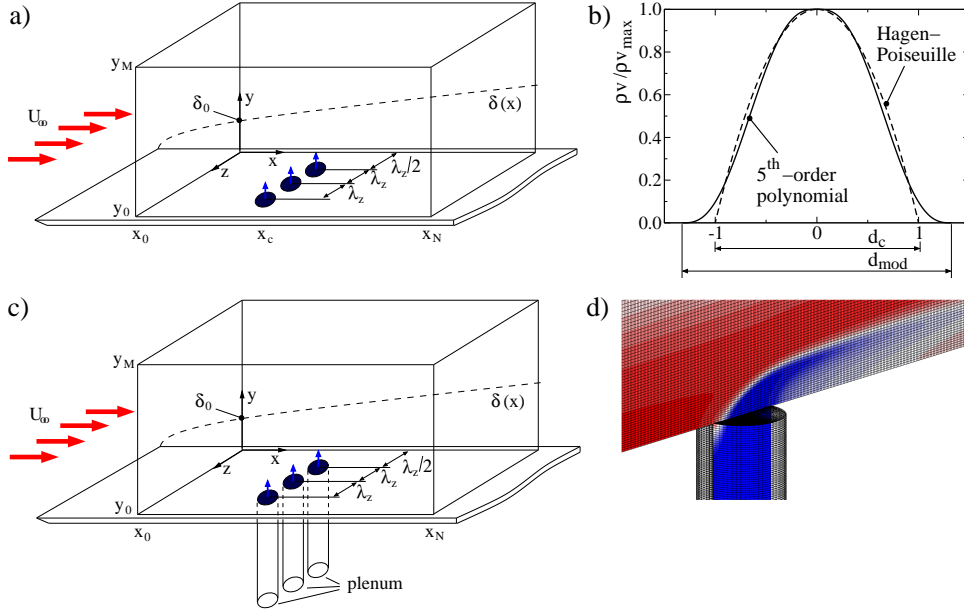


FIGURE 1. a) Integration domain for the modeled blowing. b) Mass-flux distribution along the centerline of the hole for the modeled blowing using a 5th-order polynomial. The polynomial is chosen such that the maximum and area-averaged mass flux are identical to the mass-flux in an assumed Hagen-Poiseuille flow. c) Integration domain for the simulated blowing. d) Temperature distribution in the center plane $z = 0$.

pressure, ρ indicates the density, T is the temperature, and t denotes the time. The non-dimensional parameters are the Mach number Ma , the Prandtl number Pr and the Reynolds number Re . The latter is defined as $Re = (\rho_\infty^* \cdot u_\infty^* \cdot L^*) / (\mu_\infty^*)$ and set to $Re = 10^5$. \mathbf{I} is the identity matrix. The subscript ∞ refers to freestream values and the asterisk $*$ labels dimensional quantities.

2.2. Computational domain, boundary conditions and simulation setup

In the present work, a laminar boundary-layer flow over a flat plate at a Mach number of $Ma = 2.67$ with zero pressure gradient is investigated. Figure 1-a) shows the rectangular integration domain. For the simulated blowing additional cylindrical domains are attached to the main computational domain, using bilinear interpolation in the wall plane for coupling. This is illustrated in Figures 1-c) and 1-d). A time-accurate direct numerical simulation (DNS) is used to compute the flow quantities. A DNS solves the governing equations without turbulence modeling and allows for detection of any enhanced laminar-flow instability leading to self-excited unsteadiness. The code uses splitted compact finite differences of 6th-order in streamwise and wall-normal direction and a Fourier spectral ansatz in spanwise direction, due to the assumed periodicity of the flow field. The classical explicit 4th-order Runge-Kutta procedure is applied for the integration in time. For more details concerning the numerical solver see [9].

A self-similarity solution of boundary-layer theory provides the flow variables which are prescribed at the inflow ($x = x_0$). At the outflow ($x = x_N$), a buffer region is used, where all instantaneous flow variables are smoothly ramped to the baseflow solution [9]. At the wall ($y = y_0$), the no-slip, no-penetration boundary conditions are imposed on the

velocity components. The pressure is calculated according to $\partial p / \partial y|_w = 0$ and the density is computed from the equation of state. Both an adiabatic and isothermal-wall boundary condition are investigated. Note that thermal conduction within the wall is neglected in this study. At the freestream boundary ($y = y_M$), all flow variables are computed such that the gradient along spatial characteristics is zero, except for the pressure which is computed from the equation of state.

The modeled blowing is realized by prescribing the mass flux and temperature distribution over the holes using a polynomial of 5th-order [2]. In order to specify the same maximum and area-averaged mass flux as in an assumed Hagen-Poiseuille flow through a blowing channel the modeled radius r_{mod} has to be larger than the real radius of the hole r_c ($r_{mod} = \sqrt{7/4} \cdot r_c$, see Figure 1 b)). The mass-flux distribution is given by $(\rho v)_c = (\rho v)_{max} \cdot c(r)$, where $(\rho v)_{max}$ is the maximum mass flux in wall-normal direction and $c(r)$ describes a polynomial of 5th-order, where both the gradient and curvature are zero at $r = 0$ and $r = r_{mod}$:

$$c(r) = 1 - 6 \cdot \left(\frac{r}{r_{mod}}\right)^5 + 15 \cdot \left(\frac{r}{r_{mod}}\right)^4 - 10 \cdot \left(\frac{r}{r_{mod}}\right)^3, \quad (2.6)$$

$$\text{with } r = \sqrt{(x - x_c)^2 + (z - z_c)^2}, \quad 0 \leq r \leq r_{mod}.$$

In equation (2.6), x_c and z_c describe the coordinates of the hole center, x and z indicate the position of each grid point at the wall for which the blowing ratio is computed. Similarly, the temperature distribution over the holes is given by

$$T_c = T_s \cdot (1 - c(r)) + T_{c,core} \cdot c(r), \quad (2.7)$$

where T_s represents the temperature at the hole edge and $T_{c,core} = 293[K]$ is the core temperature of the cold air at the hole center.

For simulated blowing the singularity at the rotation axis $r = 0$, which occurs due to the use of finite differences, is treated according to Mohseni and Colonius [10]. Here, the discretization is chosen such that no grid points are placed on the singularity axis. Furthermore, mode reduction in circumferential direction is applied for the Fourier spectral ansatz in order to keep the time step within a reasonable limit. At the bottom of the cylindrical domain a constant plenum pressure and plenum temperature are prescribed. The density is computed from the equation of state and the v -velocity is extrapolated from the flow field within the channel. The velocity components in radial and azimuthal direction are set to zero. A Hagen-Poiseuille flow serves as an initial condition for the channel flow. The channel has a length of $l = 2.457[mm] \approx 10 \cdot r_c$. More details on the implementation of the cylindrical computational domain can be found in the work of Kunze [11].

For the isothermal wall three different cases are investigated: Case *IS-I-A* refers to the blowing with a plenum pressure of $p_{plenum} = 0.1639[bar]$. Case *IS-I-B* labels the modeling with an increased plenum pressure of $p_{plenum} = 0.1760[bar]$. Finally, Case *IS-II* represents the blowing through two rows of staggered holes with a plenum pressure of also $p_{plenum} = 0.1760[bar]$. For the adiabatic-wall boundary condition two different cases are presented: Case *AD-I* indicates the blowing through one row of holes and case *AD-II* refers to the blowing through two rows of staggered holes. Both simulations

case notation	plenum pressure	temperature modeling	mass-flux modeling
<i>IS-I-A</i>	0.1639 [bar]	-	O5-pol. (adapted to sim. blowing)
<i>IS-I-B</i>	0.1760 [bar]	-	O5-pol. (adapted to sim. blowing)
<i>IS-II</i>	0.1760 [bar]	-	O5-pol. (adapted to sim. blowing)
<i>AD-I</i>	0.1639 [bar]	MOD-A:	O5-pol. O5-pol. (adapted to sim. blowing)
		MOD-B:	Top-hat O5-pol. (adapted to sim. blowing)
<i>AD-II</i>	0.1639 [bar]	MOD-A:	O5-pol. O5-pol. (adapted to sim. blowing of <i>AD-I</i>)
		MOD-B:	Top-hat O5-pol. (adapted to sim. blowing of <i>AD-I</i>)
		MOD-C:	Top-hat O5-pol. (adapted to sim. blowing)

TABLE 1. Cases considered.

Freestream Mach number Ma_∞	2.67	[-]		
Freestream temperature T_∞	1.00	[-]	564.0	[K]
Freestream pressure p_∞	0.10	[-]	0.1489	[bar]
Adiabatic wall temperature T_{aw}	2.20	[-]	1241.58	[K]
Isothermal wall temperature T_{iw}	0.52	[-]	293.0	[K]
Reference length L	1.00	[-]	24.57	[mm]
Hole radius r_c	0.0102	[-]	0.250	[mm]
Modeled hole radius r_{mod}	0.0135	[-]	0.331	[mm]
Distance from the leading edge $x_{c,1}$	2.2390	[-]	55.00	[mm]
Distance from the leading edge $x_{c,2}$	2.2710	[-]	55.80	[mm]
Channel length l	0.10	[-]	2.457	[mm]
Plenum pressure p_{plenum}	0.110/0.118	[-]	0.1639/0.1760	[bar]
Plenum temperature T_{plenum}	0.52	[-]	293	[K]
Streamwise spacing s_x	0.0325	[-]	0.8	[mm]
Spanwise spacing s_z	0.0325	[-]	0.8	[mm]
Periodicity length λ_z	0.0325	[-]	0.8	[mm]
$N_x \times N_y \times N_z$	2000 x 151 x 64	[points]		
Δx	$0.500 \cdot 10^{-3}$	[-]		
$\Delta y_0 - \Delta y_M$	$0.500 \cdot 10^{-3} - 2.117 \cdot 10^{-3}$	[-]		
Δz	$0.509 \cdot 10^{-3}$	[-]		
$N_r \times N_h \times N_\varphi$	41 x 200 x 64	[points]		
Δr	$0.250 \cdot 10^{-3}$	[-]		
Δh	$0.500 \cdot 10^{-3}$	[-]		
$\Delta \varphi$	$2\pi/64$	[-]		
Δt	$0.982 \cdot 10^{-4}$	[-]		
$y_0 - y_M$	0.000 - 0.166	[-]		
$x_0 - x_N$	1.600 - 2.600	[-]		

TABLE 2. Simulation setup parameters.

are performed at a plenum pressure of $p_{plenum} = 0.1639[\text{bar}]$. Note that the abbreviation 'IS' refers to 'isothermal' and 'AD' stands for adiabatic. 'I' and 'II' label the number of rows. Table 1 summarizes all investigated cases and Table 2 contains an overview of the simulation setup. The values are consistent with the experiment and previous numerical investigations [2–4].

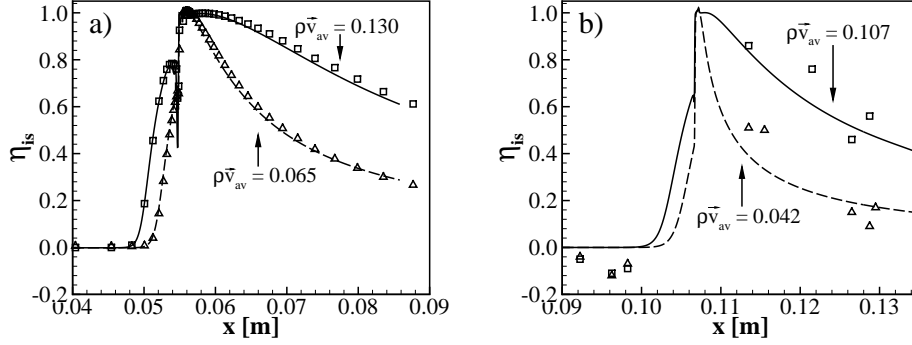


FIGURE 2. Comparison of the isothermal cooling effectiveness. a) DNS (–) vs. finite-volume solver [7] (symbols), $Ma_\infty = 2.60$, $T_\infty = 488[K]$, $p_\infty = 0.1375[bar]$, $x_c = 0.055[m]$, $\alpha_c = 90^\circ$. b) DNS (–) vs. experiment [6] (symbols), $Ma_\infty = 2.61$, $T_\infty = 545[K]$, $p_\infty = 0.15[bar]$, $x_c = 0.107[m]$, $\alpha_c = 45^\circ$.

3. Results

3.1. Code Validation

For validation purposes a comparison with the numerical results of Dahmen, Gotzen & Müller [7] and the experimental findings of Hombusch & Olivier [6] is performed. According to the experiment the wall is isothermal, $T_w = 293[K]$, and the streamwise pressure gradient is zero. Figure 2 shows the cooling effectiveness for blowing through infinite spanwise slits for various blowing ratios. The isothermal cooling effectiveness is defined as $\eta_{is} = 1 - \dot{q}_c / \dot{q}_{uc}$, where \dot{q}_c and \dot{q}_{uc} label the heat-flux distribution for the cases with and without cooling, respectively. The comparison with the multiresolution finite-volume solver of [7] is carried out for a slit position of $x_c = 0.055[m]$ and perpendicular blowing with $\alpha_c = 90^\circ$. For the comparison with the experiment, the blowing is performed at an angle of $\alpha_c = 45^\circ$ and a slit position of $x_c = 0.107[m]$. The blowing ratio is given by $(\rho\vec{v})_{av} = (\rho\vec{v})_{av}^* / (\rho U)_\infty$ which corresponds to the integral mass flux, based on the velocity in blowing direction (\vec{v}). Both plots show good agreement. It can therefore be concluded that the code is well suited for the computation of film cooling in a supersonic flat-plate boundary layer. Note that the isothermal case with a coolant gas temperature equal to the cooled-wall temperature is a special case: It ensures the laminarity of the boundary layer.

3.2. Modeled versus Simulated Blowing

3.2.1. Grid Independence

At first, the influence of the grid resolution is investigated in order to exclude grid dependence. The results of the simulations for case *AD-I* with a coarse and fine spanwise resolution ($\Delta z_{fine} = 0.5 \Delta z_{coarse}$) are illustrated in Figure 3, where the u - and T -profiles at $x = x_c$ as well as the mass-flux distribution along the centerline of the hole at $y = 0.0$ are displayed. It can be seen that all three quantities show a very good agreement and the results are therefore considered to be grid independent. In the following, all simulations are performed on the computational grid of the coarse simulation with $2000 \times 151 \times 64$ points in x -, y - and z -direction, respectively, for the main computational domain and $41 \times 200 \times 64$ points in r -, h - and φ -direction, respectively, for the cylindrical domain.

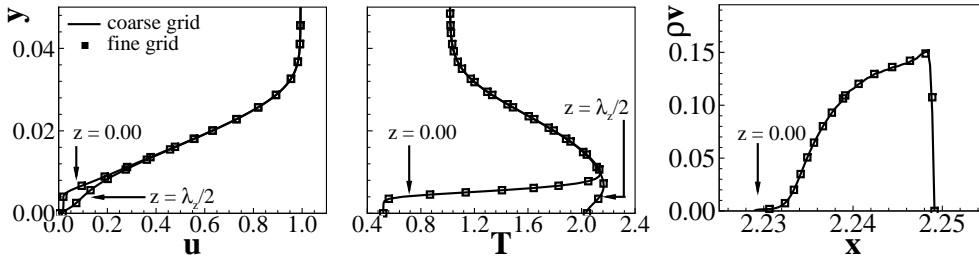


FIGURE 3. u -velocity and temperature profiles at $x = x_c$ as well as mass flux distribution at $z = 0$ and $y = 0$ for the coarse and fine z -grid resolution. Simulated blowing, case *AD-I*, $\Delta z_{fine} = 0.5 \cdot \Delta z_{coarse}$.

3.2.2. Isothermal Wall

The mass flux and temperature distribution along the centerline of the holes for the modeled and simulated blowing of the three investigated cases is presented in Figure 4. It can be observed that the mass-flux distribution at the connection between flat plate and channel ($y = 0.0$) strongly differs from the distribution at the plenum ($y = -0.1$). For all three cases, the maximum mass flux occurs at the downstream edge of the holes due to the influence of the main flow. The figure also illustrates that despite the same plenum pressure at both rows for case *IS-II*, the mass-flux through the first row is significantly lower than through the second row. For the modeled blowing the mass-flux distribution is chosen such that it matches the Hagen-Poiseuille-profile at the plenum in matters of maximum and area-averaged values. Note that for the blowing through two rows this approach relies on the knowledge of the values obtained from the simulated blowing. It is not possible to determine the mass-flux distribution a priori, since it is depending on the streamwise and spanwise spacing of the holes as well as on the plenum pressure and the boundary layer state. Note that a temperature variation can be observed for the simulated blowing at $y = 0.0$ which cannot be considered in the modeled case. Instead, a constant temperature equal to the wall temperature is prescribed in the region of the holes.

Figure 5 shows the spanwise-averaged pressure distribution at the wall for case *IS-II*. It demonstrates that the first row of holes is strongly influenced by the presence of the second row, since the blowing acts like an obstacle in the flow. Hence, the wall pressure in the region is increased leading to a reduction of the driving pressure difference between the plenum and the freestream for the first row of holes. As a result, the mass-flux distribution for the blowing through the first row is significantly lower than through the second row of holes.

Isocontours of the cooling effectiveness as well as the spanwise averaged cooling effectiveness for the three investigated cases are illustrated in Figure 6. The isocontour plots reveal that the agreement between the modeled and simulated blowing is very good for case *IS-I-A* and the difference in the spanwise averaged cooling effectiveness is negligible for large x . However, the discrepancies between the modeled and simulated blowing increase as the blowing ratio is increased. The streaky structures are significantly more pronounced resulting in both lower minimum and higher maximum values in downstream direction. This is also illustrated in the spanwise averaged values,

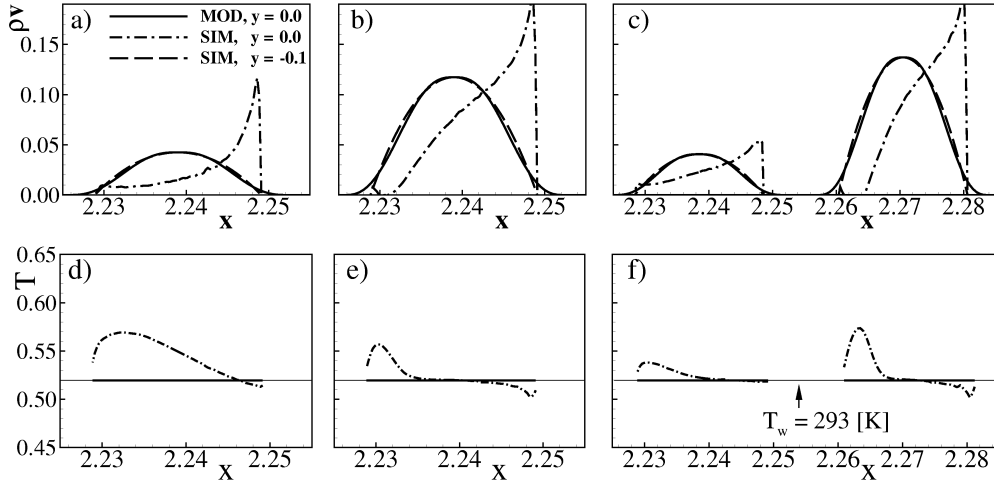


FIGURE 4. Mass-flux distribution, a)-c), and temperature distribution, d)-f), for the modeled and simulated blowing along the centerline of the holes at $y = 0.0$ and $y = -0.1$. From left to right: Case *IS-I-A*, case *IS-I-B* and case *IS-II*.

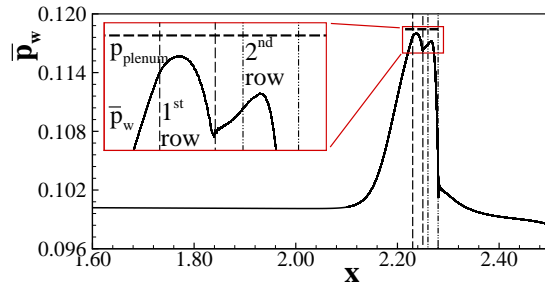


FIGURE 5. Spanwise averaged wall pressure for the simulated blowing, case *IS-II*.

where the difference between the simulated and modeled blowing is particularly large right downstream of the holes. The strongest difference can be observed for blowing through two staggered rows of holes, although the modeled mass flux is chosen such that it corresponds to the simulated mass flux for both the first and second row of holes (see Figure 4). The strong deviation in the mass-flux distribution at $y = 0$ is held responsible for this behavior. Due to the influence of the main flow the maximum mass flux of the coolant gas is shifted towards the downstream edge of the holes resulting in a higher cooling effectiveness in the near-downstream region. This effect is more pronounced as the blowing ratio / plenum pressure is increased. As pointed out in [2], the modeled-blowing approach typically gives a lower bound for the cooling efficiency.

Figure 7 shows vortex visualizations of the developing flow structures using constant values of λ_2 [12]. The shading refers to the spanwise vorticity, where white indicates a clockwise rotation when looking downstream and black labels a counterclockwise rotation of the vortices. All three cases exhibit similar flow structures. For case *IS-I-B* two characteristic vortical structures can be observed: The horse shoe vortex pair (HSVP) and the more dominant counter rotating vortex pair (CVP). All investigated cases illus-

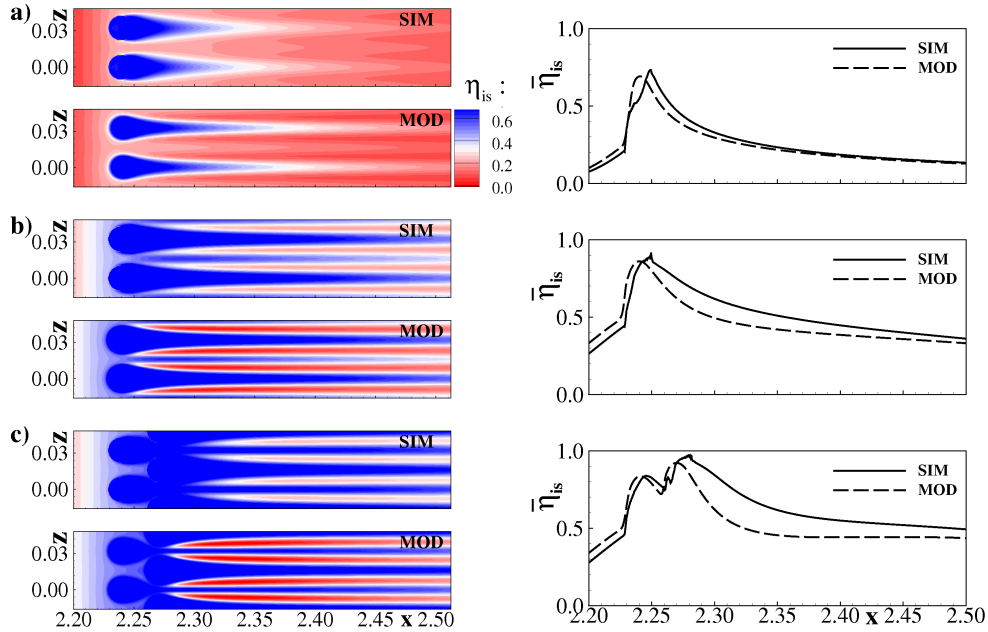


FIGURE 6. Isolines of cooling effectiveness and spanwise averaged cooling effectiveness for the modeled and simulated blowing. a)-c) Case *IS-I-A*, case *IS-I-B* and case *IS-II*.

trate that the vortical structures are slightly more pronounced for the modeled blowing. This is also illustrated in Figure 8, where a spanwise crosscut through the temperature field and isolines of the streamwise velocity are shown for the downstream position $x = 2.3$.

3.2.3. Adiabatic Wall

For the adiabatic wall not only the modeling of the mass flux is of importance but also the modeling of the temperature distribution is found to play a major role. It can be observed that the latter has a significant influence on the developing flow structures and the cooling effectiveness. Three different modeling approaches are used for comparison with the simulated blowing. Case *MOD-A* refers to the modeled blowing, where both the mass flux and the temperature distribution in the region of the holes are prescribed using a 5^{th} -order polynomial taking into account the variable temperature at the hole edge. In case *MOD-B* the mass flux is given by the 5^{th} -order polynomial, but now a top-hat profile is used for the temperature modeling. Note that the temperature corresponds to the plenum temperature. For blowing through two staggered rows of holes the mass flux distribution is the same for both rows and identical to the single row case. In contrast to both cases *MOD-A* and *MOD-B*, case *MOD-C* is characterized by a low blowing ratio through the first row of holes and high blowing ratio through the second row. The mass-flux distribution relies on the results of the simulated blowing and is prescribed by the 5^{th} -order polynomial. The temperature modeling is realized by means of the top-hat profile.

The temperature and mass-flux distribution along the centerline of the holes is presented in Figure 9. For blowing through one row of holes (case *AD-I*, Figure 9-a,b) the graph shows a comparison of the simulated blowing with cases *MOD-A* and *MOD-B*.

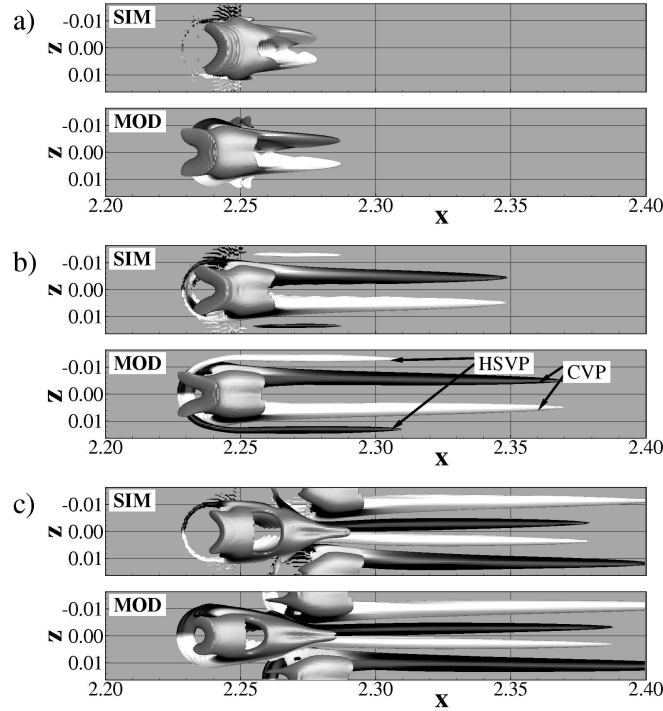


FIGURE 7. Vortex visualization (top view) using isosurfaces of $\lambda_2 = -5$ for the modeled and simulated blowing. The shading refers to the spanwise vorticity. a)-c) Case *IS-I-A*, case *IS-I-B* and case *IS-II*.

It can be observed that the coolant jet is notably too warm for case *MOD-A*. Due to the adiabatic channel wall the temperature of the coolant gas is identical to the plenum temperature for the most part of the channel. This legitimates the assumption of a top-hat profile for the temperature modeling. As for the isothermal case, the maximum mass flux occurs at the downstream edge of the hole. For blowing through two staggered rows of holes (case *AD-II*, Figure 9-c)) the results obtained from the simulated blowing are compared to case *MOD-C*. As reported for the isothermal wall boundary condition the mass flux through the first row of holes is significantly lower than through the second row. Again, this can be explained by the increasing wall pressure in front of the holes, which act as obstacles in the flow and lead to a decrease in the effective pressure difference between plenum and freestream for the first row of holes. This is illustrated in Figure 10.

Isolines of the adiabatic cooling effectiveness for the modeled and simulated blowing are shown in Figure 11. For visualization purposes the graph also contains the corresponding spanwise averaged values. The cooling effectiveness for an adiabatic wall is defined as $\eta_{ad} = (T_{aw,uc} - T_{aw,c}) / (T_{aw,uc} - T_{c,core})$. In this equation $T_{aw,uc}$ refers to the adiabatic wall temperature with the blowing turned off (uncooled), $T_{aw,c}$ indicates the wall temperature of the cooled wall, and $T_{c,core} = 293[K]$ labels the temperature of the coolant gas. A comparison of the investigated cases reveals that for blowing through one row of holes the agreement between the modeled and the simulated blowing is very poor when the 5th-order polynomial temperature modeling is employed (case *MOD-A*). In contrast, when using the top-hat profile for the temperature modeling (case *MOD-*

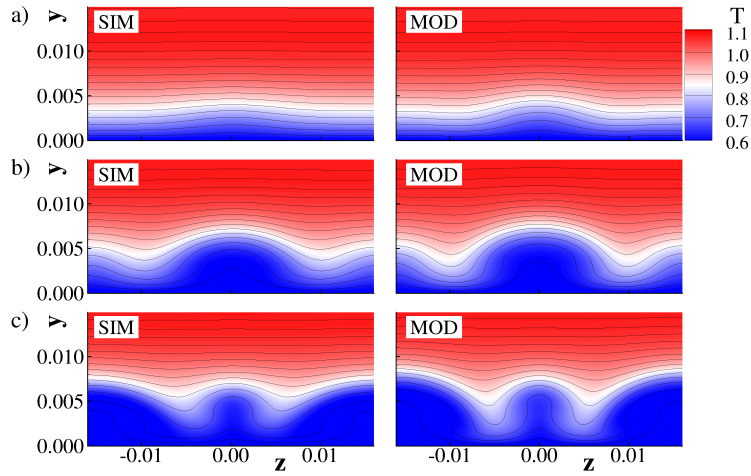


FIGURE 8. Spanwise crosscut of the temperature field with isolines of u -velocity ($0.0 < u < 1.0$, $\Delta u = 0.05$) for the modeled and simulated blowing at $x = 2.3$. a)-c) Case *IS-I-A*, case *IS-I-B* and case *IS-II*.

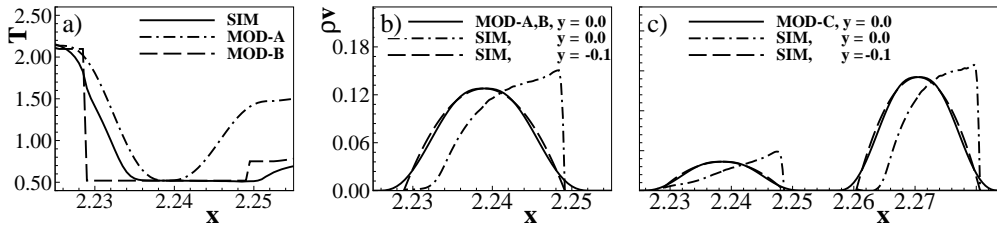


FIGURE 9. a) Temperature distribution at $y = 0.0$. b,c) Mass-flux distribution at $y = 0.0$ and $y = -0.1$. The results are taken at the centerline of the holes for both the modeled and simulated blowing. a,b) Case *AD-I* and c) case *AD-II*.

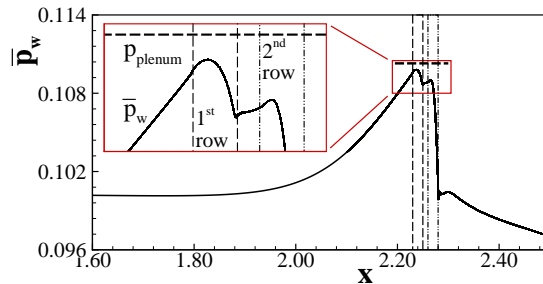


FIGURE 10. Spanwise averaged wall pressure for the simulated blowing, case *AD-II*.

B) the agreement with the simulated blowing is considerably better. Now, the developing structures are quite similar and the spanwise averaged cooling effectiveness is just slightly lower than the values obtained from the simulated blowing.

For blowing through two staggered rows of holes it can be observed that the first row does not much contribute to the cooling of the flat plate due to the significantly lower amount of injected coolant. Figure 11 demonstrates that case *MOD-C* results in a good

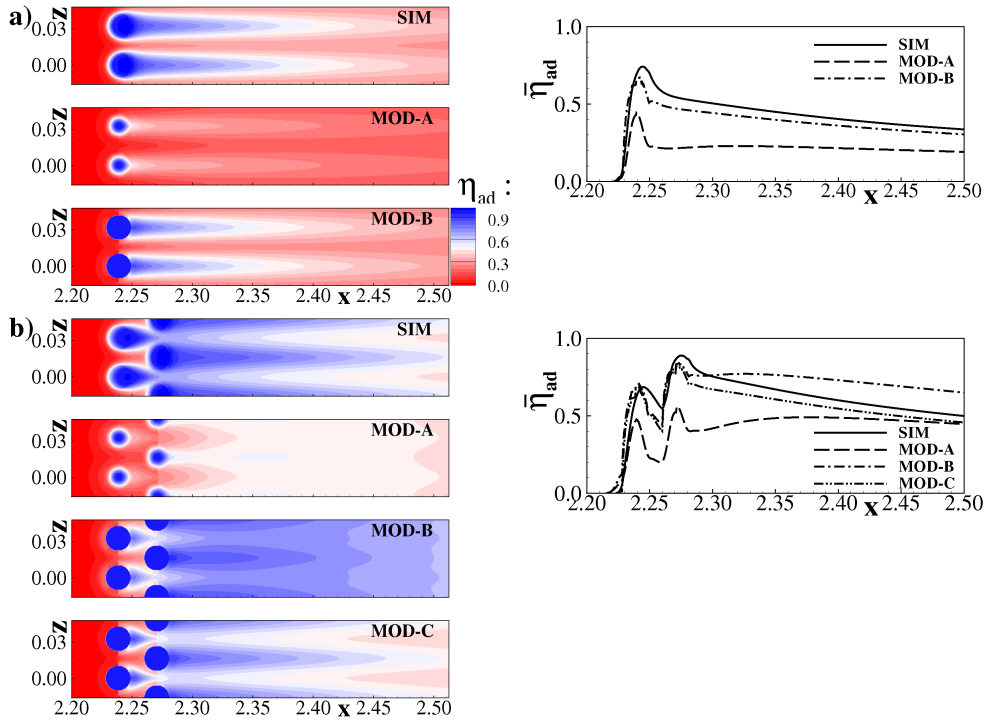


FIGURE 11. Isolines of cooling effectiveness and spanwise averaged cooling effectiveness for the modeled and simulated blowing. a) Case *AD-I* and b) case *AD-II*.

agreement with the simulated blowing. The developing structures are quite similar and the spanwise averaged cooling effectiveness is just marginally lower. In contrast to that, the cooling effectiveness for case *MOD-A* is much lower than for the case with simulated blowing. Despite the stronger blowing ratio ($rv_{max} = 0.128$ at both holes) and, thus, the greater amount of injected cooling gas, the higher temperature of the jet can be held responsible for this behavior. The use of the top-hat profile for the temperature modeling (*MOD-B*), however, results in a cooling effectiveness that is much too high. Here, the modeled blowing ratio (also $rv_{max} = 0.128$ at both holes) significantly overestimates the simulated blowing. However, it is not clear whether the assumption of a constant 'plenum' pressure for each channel blowing holds in reality or not.

The developing flow structures visualized by constant values of λ_2 for the adiabatic-wall boundary condition are shown in Figure 12. For case *AD-I* the flow structures obtained from case *MOD-B* are in very good agreement with the simulated blowing, whereas case *MOD-A* demonstrates a slightly more pronounced counter-rotating vortex pair. This illustrates that the temperature distribution of the coolant has a notable influence on the flow structures. Due to the strong difference between the blowing ratios of the first and second row of holes for case *AD-II* the counter-rotating vortex pair of the first row of holes is negligible. This behavior is best represented by case *MOD-C*, which shows a very good agreement with the simulated blowing. In contrast, cases *MOD-A* and *MOD-B* exhibit a counter-rotating vortex pair emerging from the first row of holes, which is due to the higher blowing ratio of row one.

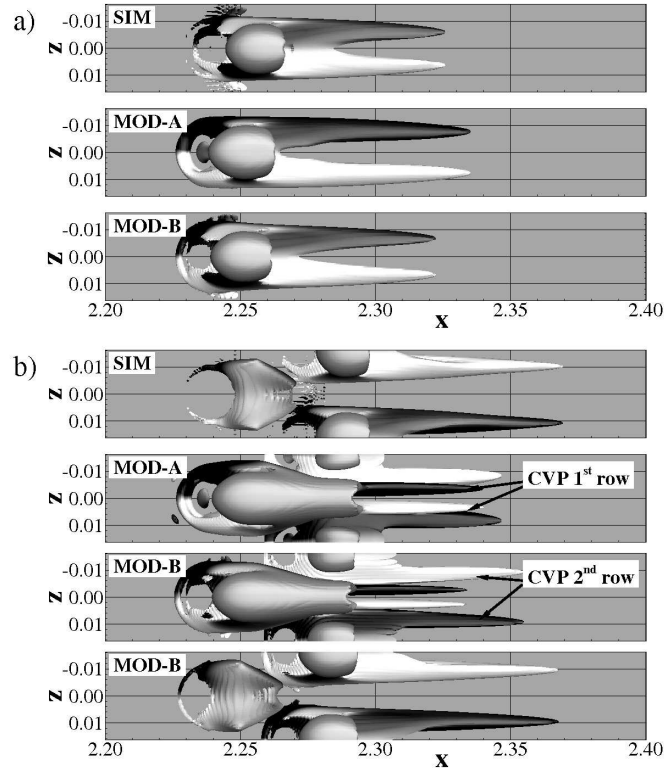


FIGURE 12. Vortex visualization (top view) using isosurfaces of $\lambda_2 = -5$ for the modeled and simulated blowing. The shading refers to the spanwise vorticity. a) Case *AD-I* and b) case *AD-II*.

A spanwise crosscut of the temperature flow field with isolines of constant u -velocity is presented in Figure 13. It illustrates that the agreement between the simulated blowing and case *MOD B* is very good for the blowing through one row of holes. For the blowing through two staggered rows of holes the best agreement with the simulated blowing can be observed for case *MOD-C*, which, in contrast to case *MOD-B*, takes into account the different blowing ratios through the first and second row of holes.

4. Conclusions

The present work is dedicated to the evaluation of the modeled blowing approach for film cooling in a laminar Mach-2.67 boundary layer with an adiabatic and isothermal wall boundary condition. This is realized by comparison with a numerical setup where the cylindrical blowing channel is simulated and coupled to the main computational domain. For the isothermal wall it is found that the spanwise averaged cooling effectiveness obtained from the modeled blowing is lower in the near-downstream region of the holes than the values obtained from the simulated blowing. This effect is less pronounced for a lower blowing ratio and, also, for the region far downstream of the holes, where both the modeled and simulated blowing are in good agreement. Moreover, the developing flow structures of the modeled blowing are slightly more pronounced due to the devi-

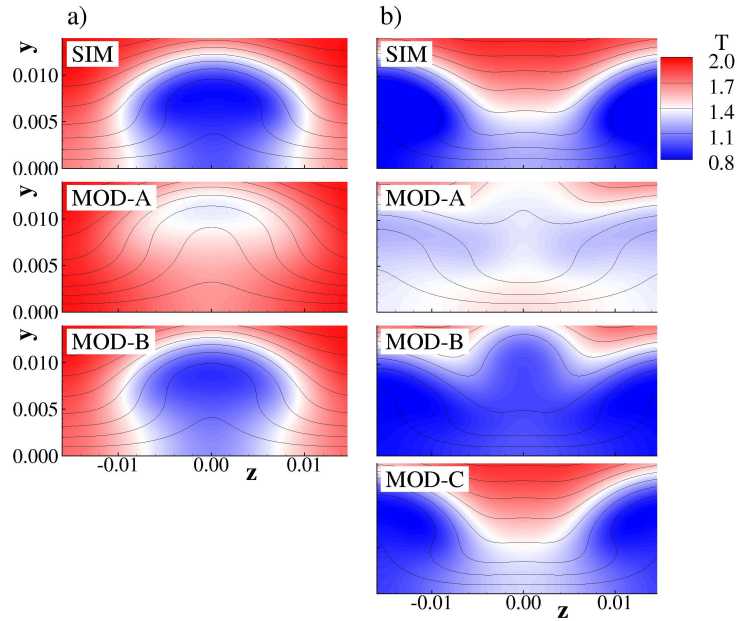


FIGURE 13. Spanwise crosscut of the temperature field with isolines of u -velocity ($0.0 < u < 1.0$, $\Delta u = 0.05$) for the modeled and simulated blowing. a) Case *AD-I* at $x = 2.3$ and b) case *AD-II* at $x = 2.325$.

ating mass-flux distribution across the holes. For the blowing through two staggered rows of holes it was shown that the mass flux through the first row is significantly lower than through the second row, provided that the 'plenum' pressure at the lower end of each blowing channel is the same. This can be explained by the increased wall pressure, since the holes are acting as obstacles in the flow. Hence, the modeling of the mass flux for blowing through two or more rows of holes relies on the knowledge of the simulated-blowing results. For the adiabatic-wall boundary condition the modeling of the temperature distribution plays an important role. Here it was demonstrated that the use of a top-hat profile for the temperature modeling of the coolant gas is superior to the previously used 5th-order polynomial. The adiabatic channel wall preserves the plenum temperature of the coolant gas on its way through the blowing channel. Thus, the top-hat profile temperature-modeling results in a better agreement with the simulated blowing. At the blowing ratios considered no induced global instability of the laminar flow could be observed. Future work is going to focus on the influence of a transitional and turbulent boundary layer state.

Acknowledgments

The financial support of the German Research Foundation (DFG) in the framework of the collaborative research center Transregio 40 (SFB-TRR-40) and the computational resources, kindly provided by the Federal High Performance Computing Center Stuttgart (HLRS), are gratefully acknowledged.

References

- [1] LINN, J. AND KLOKER, M.J. (2008). Numerical Investigations of Film Cooling and its Influence on the Hypersonic Boundary-Layer Flow. In: Gülhan, A. (Ed.), *RESPACE - Key Technologies for Reusable Space Systems, NNFM*, **98**, 151–169, Springer.
- [2] LINN, J. AND KLOKER, M.J. (2011). Effects of Wall-Temperature Conditions on Effusion Cooling in a Mach-2.67 Boundary Layer. *AIAA-J.*, **49**(2), 299–307, DOI: 10.2514/1.J050383.
- [3] LINN, J., KELLER, M. AND KLOKER, M.J. (2010). Effects of Inclined Blowing on Effusion Cooling in a Mach-2.67 Boundary Layer. *Sonderforschungsbereich/Transregio 40 - Annual Report 2010*, 55–67.
- [4] HEUFER, K.A. AND OLIVIER, H. (2008). Experimental Study of Active Cooling in 8 Laminar Hypersonic Flows. In: Gülhan, A. (Ed.), *RESPACE - Key Technologies for Reusable Space Systems, NNFM*, **98**, 132–150, Springer.
- [5] HEUFER, K.A. AND OLIVIER, H. (2008). Experimental and Numerical Study of Cooling Gas Injection in Laminar Supersonic Flow. *AIAA-J.*, **46**(11), 2741–2751, DOI: 10.2514/1.34218.
- [6] HOMBSCHE, M. AND OLIVIER, H. (2010). Flow condition and cooling gas variation for film cooling studies in hypersonic flow. *Sonderforschungsbereich/Transregio 40 - Annual Report 2010*, 27–39.
- [7] DAHMEN, W., GOTZEN, T. AND MÜLLER, S. (2009). Numerical Simulation of Cooling Gas Injection Using Adaptive Multiscale Techniques. *Sonderforschungsbereich/Transregio 40 - Annual Report 2009*, 9–21.
- [8] WHITE, F.M. (1991). *Viscous Fluid Flow*. McGraw-Hill.
- [9] BABUCKE, A., LINN, J., KLOKER, M.J. AND RIST, U. (2003). Direct Numerical Simulation of Shear Flow Phenomena on Parallel Vector Computers. In: Resch, M. et al. (Eds.), *High Performance Computing on Vector Systems*. High Performance Computing Center, Stuttgart (HLRS), 229–247. Springer.
- [10] MOHSENI, K. AND COLONIUS, T. (2000). Numerical Treatment of Polar Coordinate Singularities. *J. Comput. Phys.*, **157**, 787–795.
- [11] KUNZE, P. (2009). *Numerische Untersuchungen des Einflusses von Ausblasekanälen auf die Filmkühlung im Überschall*. Studienarbeit, Universität Stuttgart.
- [12] JOENG, J. AND HUSSIAN, F. (1995). On the Identification of a Vortex. *J. Fluid Mech.*, **285**, 69–94.